nuclear fusion
IAEA

PAPER

# Experimental observation of electron-scale turbulence evolution across the L–H transition in the National Spherical Torus Experiment

To cite this article: Y. Ren *et al* 2019 *Nucl. Fusion* **59** 096045

View the article online for updates and enhancements.

This content was downloaded from IP address 198.125.231.54 on 14/08/2019 at 15:07

IOP Publishing | International Atomic Energy Agency Nuclear Fusion

Nucl. Fusion **59** (2019) 096045 (14pp) https://doi.org/10.1088/1741-4326/ab2f4f

# Experimental observation of electron-scale turbulence evolution across the L–H transition in the National Spherical Torus Experiment

**Y. Ren[1,a], D.R. Smith[2], S.J. Zweben[1], R. Bell[1], W. Guttenfelder[1], S.M. Kaye[1], B.P. LeBlanc[1], E. Mazzucato[1], K.C. Lee[3], C.W. Domier[4], P.J. Sun[5] and H. Yuh[6]**

[1] Princeton Plasma Physics Laboratory, Princeton, NJ 08543, United States of America
[2] University of Wisconsin-Madison, Madison, WI 53706, United States of America
[3] National Fusion Research Institute, Daejeon, 305-806, Korea, Republic of
[4] University of California at Davis, Davis, CA 95616, United States of America
[5] Institute of Plasma Physics, Chinese Academy of Sciences, PO Box 1126, Hefei, Anhui 230031, People's Republic of China
[6] Nova Photonics, Inc., Princeton, NJ 08540, United States of America

E-mail: yren@pppl.gov

Received 19 April 2019, revised 15 June 2019
Accepted for publication 4 July 2019
Published 6 August 2019


**Abstract**

Electron-scale turbulence (for $3 \lesssim k_\perp \rho_s \lesssim 12$) was measured during the L–H transition in the National Spherical Torus Experiment (NSTX) (Ono *et al* 2000 *Nucl. Fusion* **40** 557) using a coherent microwave scattering system. The measurements were carried out at a radial region adjacent to the edge transport barrier (ETB) (at smaller radius than ETB). The observed L–H transition occurred during current flattop, which facilitated the measurement of electron-scale turbulence. The measured electron-scale turbulence is observed to be quasi-stationary before the L–H transition, and an intermittent phase for electron-scale turbulence is observed after the start of the L–H transition with a gradual decrease in overall turbulence density fluctuation spectral power with intermittent large relative variations (on ~0.5–1 ms time scale) in the total spectral power. A turbulence-quiescent phase is observed following the intermittent phase, and a significant reduction in the electron-scale turbulence spectral power is only observed at lower wavenumbers, namely $k_\perp \rho_s \leqslant 9$–10, which is also seen in different operational NSTX scenarios due to different stabilization mechanisms. A recovery phase is seen after the quiescent phase, where the electron-scale density fluctuation power starts to gradually increase. Simultaneous ion-scale turbulence measurements at larger radius than the electron-scale turbulence measurement location show similar temporal behavior in ion-scale turbulence as in the measured electron-scale turbulence. These observations demonstrate that the suppression of turbulence during the L–H transition is not just limited to the ETB region. None of the measured electron-scale turbulence and ion-scale turbulence from edge into core is found to be obviously leading in the response to the L–H transition, and the overall turbulence suppression after the start of the L–H transition at different radii seems to start at the same time and is a gradual process happening on a tens-of-ms time scale. The trend of decrease in electron-scale turbulence during the L–H transition is found to be consistent with a decrease in the maximum electron-temperature-gradient linear growth rate from linear gyrokinetic stability analysis. However, the observed intermittency in electron-scale turbulence during the intermittent phase cannot be explained by the linear analysis.

[a] Author to whom any correspondence should be addressed.

 © 2019 IAEA, Vienna Printed in the UK

Keywords: electron-scale turbulence, ETG, L–H transition, spherical tokamak, NSTX, microwave scattering

(Some figures may appear in colour only in the online journal)

## 1. Introduction

Since H-mode was discovered on ASDEX [1], the L–H transition has been subjected to extensive theoretical and experimental studies in the past decades [2]. However, a comprehensive theory allowing predictions of the L–H transition, e.g. its power threshold and timing, for future fusion machines is still beyond reach. On the other hand, it is now well accepted that the L–H transition is due to the suppression of edge turbulence by the E×B shear from zonal and equilibrium flows in a narrow region inside the separatrix or the last closed flux surface (LCFS) to form an edge transport barrier (ETB), resulting in improved particle and energy confinement in contrast to L-mode [3–7]. Such a stabilization of edge turbulence during the L–H transition has been observed in different experiments (both tokamaks and stellarators) using a variety of diagnostic techniques, including reflectometry [8], forward and back coherent scattering [7, 9–11], neutral lithium beam probe [12], beam emission spectroscopy (BES) [13] and gas puff imaging (GPI) [14, 15]. In general, these early findings have shown that the suppression in the narrow region of ETB is very fast, i.e. on the time scale of about 100 $\mu$s (the same as the time scale for the ETB formation), which demonstrates the correlation between the turbulence suppression and the formation of ETB. However, what happens to plasma turbulence away from ETB in the plasma core is less clear. On one hand, it was found that density fluctuations remain unchanged right after the start of the L–H transition in some discharges and devices [8, 10, 12] and can either increase [9] or decrease [10] further into H-mode on a longer time scale (tens of ms). On the other hand, there are also measurements showing that even core density fluctuations are reduced on a fast time scale at the L–H transition on DIII-D and the National Spherical Torus Experiment (NSTX) [13, 16].

In addition, most of the aforementioned turbulence measurements across the L–H transition were focusing on low-frequency and ion-scale turbulence which is thought to be important for driving anomalous transport in fusion devices. While the importance of ion-scale turbulence in driving plasma transport is widely accepted, there is an increasing amount of evidence that electron-scale turbulence, e.g. that driven by electron-temperature-gradient (ETG) modes [17], is important in spherical tokamaks [18–21] and even in conventional tokamaks [22, 23]. Thus, it is important to experimentally study the evolution of electron-scale turbulence across the L–H transition. The measurement of electron-scale turbulence, due to the small spatial scale of the turbulence (sub-mm with typical tokamak parameters), has been a difficult problem. Although imaging turbulence diagnostics, e.g. BES [13] and phase contrast imaging (PCI) [24], have been proven successful in measuring ion-scale turbulence, it is quite difficult for imaging turbulence diagnostics to achieve the required spatial resolution and detecting sensitivity to measure electron-scale turbulence. Coherent scattering diagnostics, on the other hand, have not only been able to successfully measure ion-scale turbulence [25], but also were able to measure electron-scale turbulence [26, 27] due to its inherent nature of directly revolving wavenumber spectrum. An early study of electron-scale turbulence across the L–H transition was performed on W 7-AS with a CO2 laser scattering system [26] in dithering plasmas which repeatedly switched between L and H-mode [11]. Their measurements clearly show a fast suppression of electron-scale turbulence ($<$1 ms) at L–H transitions, although only spectral power at one frequency for one wavenumber was presented and how the total wavenumber spectrum evolves across the L–H transition is not clear. We also emphasize that all aforementioned scattering measurements were not localized, i.e. the length of scattering volume comparable to plasma minor radius, and, to determine the spatial location of the measured turbulence, indirect methods were used. However, even with these methods, it is difficult to achieve a radial localization of $\sim$10 percent of plasma minor radius. On NSTX, excellent localized scattering measurements of electron-scale turbulence was achieved with a radial resolution $\pm$2 cm (about 10 percent of minor radius) using a 280 GHz coherent microwave scattering system (the high-k scattering system) with an innovative scattering scheme [27, 28].

In this paper, we present the first detailed local measurements of electron-scale turbulence evolution across the L–H transition in NSTX [29] using the high-k scattering system. The measurements were made across the L–H transition during current flattop in two NSTX neutral beam injection (NBI) heated discharges, shots 139442 and 141698, with $B_T = 0.55$ T and $I_p = 0.9/1.1$ MA. We note that having the L–H transition occurring at the current flattop leads to a favorable Doppler frequency shift of scattering signals, which made reliable electron-scale turbulence measurements possible across the L–H transition. The local electron-scale turbulence measurements were carried out at $r/a \approx 0.71$–0.88 with the ETB located at $r/a \gtrsim 0.89$–0.9 for the two discharges, where *r/a* is the normalized minor radius with $a$ as the half width of the LCFS at mid-plane. It was found that the measured electron-scale turbulence is quasi-stationary before the L–H transition, followed by an intermittent phase where electron-scale turbulence, from the start of the L–H transition, gradually decreases in the overall turbulence spectral power with intermittent large relative variations (on $\sim$0.5–1 ms time scale) in the total spectral power. A turbulence-quiescent phase is found after the intermittent phase. We show that a reduction of electron-scale turbulence spectral power is only observed at lower wavenumbers, namely $k_\perp \rho_s \leqslant 9$–10, which is also

seen in different NSTX operational scenarios due to different stabilization mechanisms. A recovery phase is seen after the quiescent phase as plasma evolves further into H-mode, where high-k fluctuation power gradually increases. In addition, ion-scale turbulence was measured with BES [30] and GPI [31] diagnostics at the plasma edge (i.e. at larger radius compared to the electron-scale turbulence measurements) for shot 139442, and their temporal evolution is found to be similar to that of the measured electron-scale turbulence. We note that the response of the measured electron-scale turbulence outside of ETB to the L–H transition is fast (at most several ms), and we do not see an apparent delay compared to the response of the measured ion-scale turbulence to the L–H transition.

This paper is organized as follows. The experimental apparatus is presented in section 2. Experimental observations are shown in section 3, followed by comparisons with gyrokinetic linear stability analysis in section 4. Lastly, we summarize and discuss the results in section 5.

## 2. Experimental apparatus

The scattering configuration of the high-k scattering system [27] used for shot 139442 is shown in figure 1 as an example (configuration is similar for shot 141698), including the probe beam and scattered beam trajectories calculated using a ray tracing code. The high-k scattering system has five receiving channels covering a wavenumber range of 5 $\mathrm{cm}^{-1} \lesssim k_\perp \lesssim 30\,\mathrm{cm}^{-1}$ with a resolution of about $1\,\mathrm{cm}^{-1}$, and five heterodyne receivers are used detect scattered microwave, allowing the determination of the wave propagation direction of each wavenumber. We calibrated the power response of each receiving channel with a known-power solid-state microwave source. As a result, all receiving channels are relatively calibrated, although they are not absolutely calibrated for obtaining the actual density fluctuation amplitude. Since the scattered microwave power is known to be proportional to density fluctuations, it is possible for us to compare relatively the density fluctuation wavenumber spectral power across different scattering channels and at different experimental time points. The scattering system has a frequency response of about 5 MHz, which is large enough for measuring ETG turbulence (usually having a lab-frame frequency less than 5 MHz) in NSTX. The unique feature of this scattering system is the excellent radial resolution of $\triangle R \approx \pm\ 2\,\mathrm{cm}$, determined by the $1/e$ half width of the microwave beam power. A innovative tangential launching scheme along with the large toroidal curvature of NSTX due to its low aspect ratio leads to a scattering volume much smaller than that from a simple overlapping of the probe and scattering beams (see [28] for more details on this scattering scheme). This fine radial resolution allowed us to study the parametric dependence of the measured turbulence on local equilibrium quantities, e.g. $L_{T_e}$ [18] (electron temperature scale length), $L_{n_e}$ [19, 20] (electron density scale length), collisionality [20], $q$ (safety factor), and $\hat{s}$ (magnetic shear) [32].

The high-k scattering system had been improved through the years, including improvements in scattering scheme to significantly reduced stray radiation, adding remote control capability to allow between-shot adjustment of launching and receiving optics and the utilization of a 280 GHz solid-state microwave source to replace a back wave oscillator. The improvements in the scattering scheme made it possible to obtain scattering signals from all five channels simultaneously, compared to at most three channels previously only under limited circumstances [33]. The remote control capability allowed between-shot adjustments of launching and receiving optics, which made it possible to optimize scattering configuration according to realized plasma equilibria. Using a solid-state microwave source significantly improved system stability and reduced maintenance requirement. We note that due to the tangential launching scheme employed (see figure 1), the scattering system measures mostly radial wavenumber, $k_r$, and a finite but smaller binormal wavenumber, $k_\theta$, e.g. a range of $k_r\rho_s \sim 5$–13 and a range of $k_\theta\rho_s \sim 2$–4 for the experiments presented in this paper, where $\rho_s$ is the ion gyroradius with sound speed (radial and binormal directions are defined with respect to the local flux surface at the scattering location and the $\rho_s$ is calculated with locally measured $T_e$ and local magnetic field strength from equilibrium reconstruction). In figure 1, the scattered beam to channel 5 are partially blocked by the vacuum vessel and its scattering volume does not overlap with the other four channels determined by ray tracing. Thus, channel 5 is not used in the analysis presented

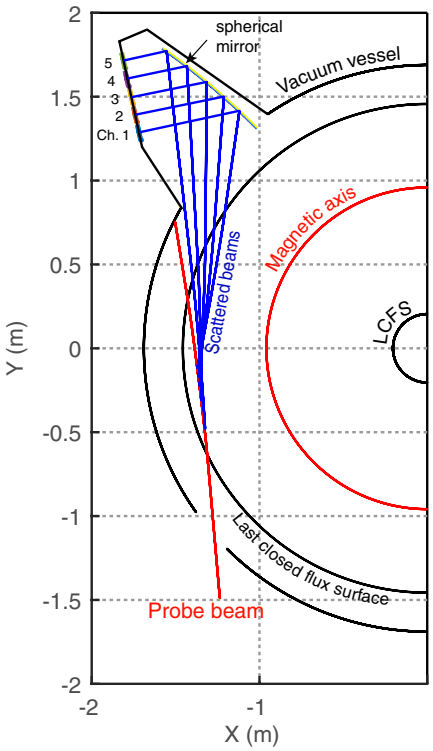


**Figure 1.** Schematic of a scattering configuration of the high-k scattering system on NSTX. The probe beam and scattered beam trajectories are calculated using a ray-tracing code for shot 139442 with measured equilibrium profiles at $t = 348$ ms. Scattered light is reflected and focused by a spherical mirror onto five collection windows.

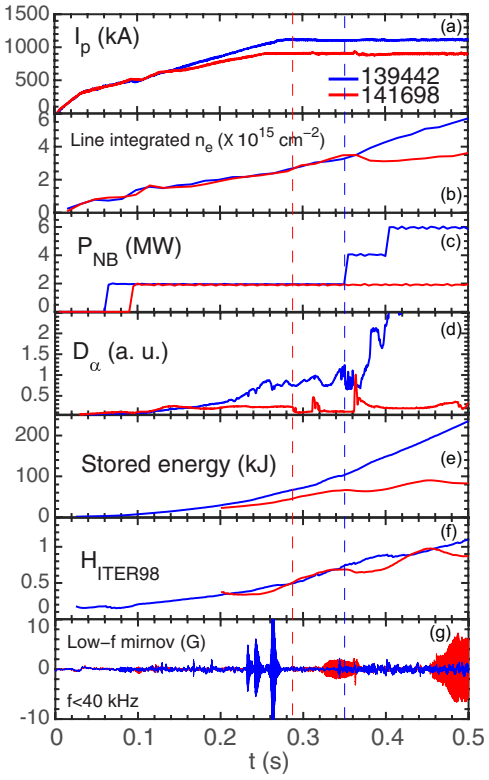


**Figure 2.** The time traces of (*a*) plasma current $I_p$, (*b*) line integrated density, (*c*) injected NBI heating power, (*d*) divertor $D_\alpha$ emission, (*e*) stored energy, (*f*) H factor and (*g*) low frequency MHD mode amplitude for shots 139442 (blue) and 141698 (red). Two dashed vertical dashed lines with the same color coding extends through all panels denote the time points of the start of the L–H transition for the two discharges.

in the paper. Furthermore, we would like to point out that although the scattering system does not capture the dominant $k_\theta$ spectral power predicted for ETG turbulence, e.g. see [34], the measured $k_\perp$ spectral power is used to assess the overall variation in the electron-scale turbulence intensity, assuming that the whole 2D wavenumber spectral power would go up or down together.

## 3. Experimental results

### 3.1. Overview

An overview of the discharges where the observation were made is shown in figure 2. The measured time traces of plasma current and line integrated density are plotted in figures 2(*a*) and (*b*) respectively. It can be seen that the current flattop starts around $t = 270$ ms with a higher current at flattop for 139442 at about 1.1 MA and a lower current at flattop for 141698 at about 900 kA. The line integrated density evolution of the two discharges is very similar until about $t = 360$ ms, after which shot 141698 had a drop in the line-integrated density because of an H–L transition, while the density for shot 139442 continued to increase. The injected NBI power waveforms are shown in figure 2(*c*), where it can be seen that shot 139442 had heating power step-ups to a maximum of 6 MW and shot 141698 had a constant NBI heating power of 2 MW. The timing of the start of the L–H transition can be identified in figure 2(*d*), where the divertor $D_\alpha$ emission time trace is shown for both discharges, from sudden drops in $D_\alpha$ emission. Two vertical dashed lines across all panels are used to denote the time of the start of the L–H transition for the discharges with the L–H transition occurring at about $t = 350$ ms and $t = 288$ ms for shots 139442 and 141698, respectively. From figure 2(*c*), it is clear that the L–H transition in shot 139442 was triggered by a NBI power step-up and the L–H transition in shot 141698 occurred more spontaneously. The stored energy (calculated using a time dependent tokamak transport and data analysis code (TRANSP) [35]) is found to continuously increase for both discharges (figure 2(*e*)), and both discharges eventually reached a H factor of 1 after the start of the L–H transition (figure 2(*f*)). Low frequency MHD activity is quite benign at the time of the L–H transition for both discharges (figure 2(*g*)), which helps us to rule out MHD activities as a source of the observed electron-scale turbulence.

To have a closer view of how equilibrium profiles vary across the L–H transition (particularly to show the formation of the ETB), time traces of $D_\alpha$ emission and electron density profiles (measured by a multi-point Thomson scattering (MPTS) system [36]) are shown in figure 3 for both discharges. A zoomed-in view of $D_\alpha$ emission is shown in figures 3(*a*) and (*c*) for shots 139442 (from $t = 330$ ms to 390 ms) and 141698 (from $t = 280$ ms to 320 ms), respectively. The start of the L–H transition can be identified from large drops in $D_\alpha$ emission seen in figures 3(*a*) and (*c*) (denoted by dashed vertical lines). It is interesting to see that after an initial fast drop (on a 1–2 ms time scale) in $D_\alpha$ after the start of the L–H transition, the $D_\alpha$ emission in both discharges does not remain low but rather has a phase of large and fast temporal variations which we name as the $D_\alpha$ dithering phase. The dithering phase of shot 139442 is obviously longer (about 12 ms) than that of shot 141698 (about 4 ms) seen in figures 3(*a*) and (*c*), which might be due to the NBI power step-up in shot 139442. From the temporal evolution of $D_\alpha$ after the start of the L–H transition in both discharges, we can see that two time scales are involved in the L–H transition: a fast time scale ($\sim$1–2 ms) for the initial strong drop of $D_\alpha$ and a slow time scale ($\sim$4–12 ms) for the dithering phase. Of course, a better determination of time scales in the L–H transition would be from the evolution of equilibrium profiles around the L–H transition. However, we did not have fast profile diagnostics in the experiments presented in the paper (the profile diagnostics used in the paper have time resolutions $\gtrsim$10 ms). Furthermore, we note that although the dithering in $D_\alpha$ after the start of the L–H transition is similar to that reported in [37], we could not determine whether the profile evolution during the dithering phase is also similar without fast profile diagnostics. These will be addressed in future experiments on NSTX-U [38]. To demonstrate the establishment of ETB, electron density profiles at two adjacent MPTS time points (one before and one after the start of the L–H transition), are shown in figures 3(*b*) and (*d*) for shots 139442 and 141698, respectively,

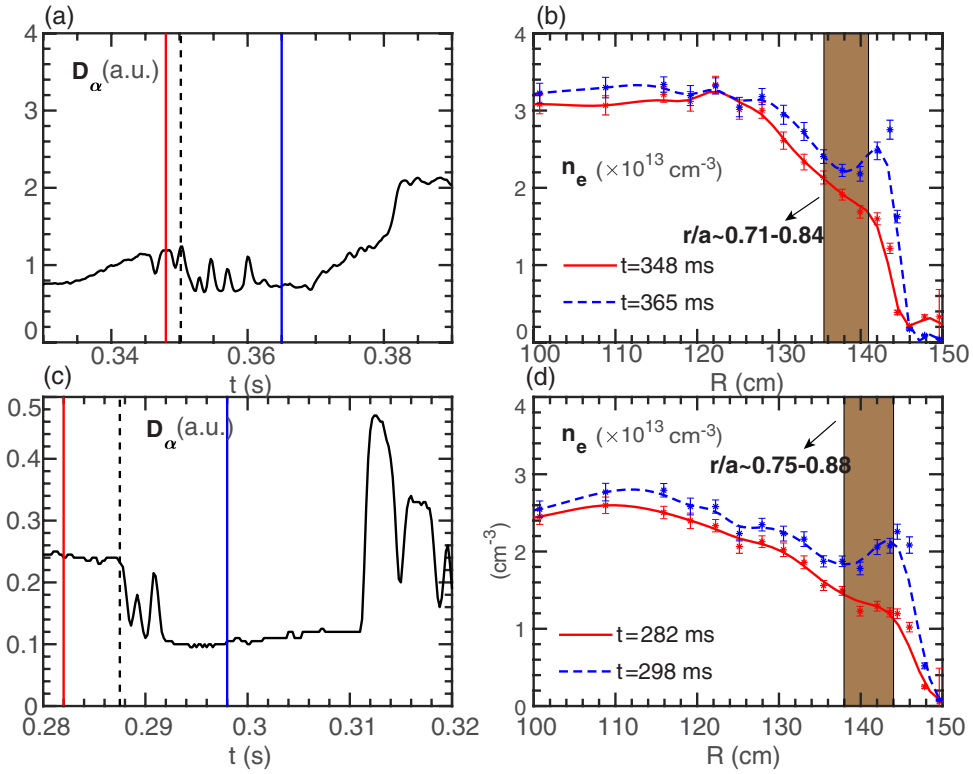


**Figure 3.** Time traces of divertor $D_\alpha$ emission for shots 139442 (*a*) and 141698 (*c*); Two electron density profiles, one before and one after the start of the L–H transition, for shots 139442 (*b*) and 141698 (*d*). The dashed vertical line in both (*a*) and (*c*) denotes the time point of the start of the L–H transition. Two colored solid vertical lines in both (*a*) and (*c*) denote the time points of two adjacent MPTS measurements around the L–H transition. The shaded rectangles in (*b*) and (*d*) denote the high-k measurement region with $r/a \approx 0.71$–$0.84$ for shot 139442 and $r/a \approx 0.75$–$0.88$ for shot 141698.

with the measurement time points denoted by solid vertical lines in figures 3(*a*) and (*c*) with same color coding. It can be clearly seen in figures 3(*b*) and (*d*) that an electron density ear developed after the start of the L–H transition and the formation of the H-mode pedestal is very evident in the density profiles. The formation of the density ear is due to the accumulation of carbon impurity at plasma edge resulting from the formation of ETB after the start of the L–H transition. We note that electron temperature also increased across the whole plasma minor radius after the start of the L–H transition (not shown). The measurement region of the high-k scattering system is denoted by a shaded rectangle in both figures 3(*b*) and (*d*), i.e. $r/a \approx 0.71$–$0.84$ for shot 139442 ($R \approx 135.5$ cm to 141 cm) and $r/a \approx 0.75$–$0.88$ for shot 141698 ($R \approx 138$ cm to 144 cm). The high-k measurement region for shot 141698 covers the H-mode pedestal top, while the high-k measurement region for shot 139442 is more toward the core of the plasma and is adjacent to the pedestal top.

### 3.2. Electron-scale turbulence evolution

The temporal evolution of electron-scale turbulence across the L–H transition is shown in figure 4, where spectrogram of two scattering channels (channels 2 and 3 of the high-k scattering system), the total scattering power and the divertor $D_\alpha$ signals are plotted in sync to elucidate the electron-scale turbulence evolution (figures 4(*a*) for shot 139442 and (*b*) for shot 141698) with a vertical solid line denoting the time of the start of the L–H transition in both figures 4(*a*) and (*b*). We note that channels 2 and 3 were configured to measure normalized wavenumbers of $k_\perp \rho_s \sim 8$–$9$ and $k_\perp \rho_s \sim 6$–$7$, respectively, across the L–H transition. In figure 4(*a*), the spectrograms of the scattering signal from channels 2 and 3 of the high-k scattering systems are shown in the two top panels. The scattering signal is identified as spectral peaks at $f > 0$ in the spectrograms ($f$ is frequency), while the central peak at $f = 0$ is due to the stray radiation (unscattered microwave from the probe beam). It can be seen that during the whole time range shown in the spectrograms, the scattering signal can be easily distinguished from the stray radiation, benefiting from the favorable Doppler frequency shift during the current flattop which shifts the scattering signal spectral peak away from the stray radiation spectral peak at $f = 0$, e.g. the frequency spectral peak around 500 kHz just before the L–H transition and the spectral peak around 1 MHz at $t = 382$ ms seen in figure 4(*a*). We note that this clear separation cannot be obtained when the L–H transition occurs earlier in a NSTX discharge during current ramp-up phase due to the insufficient Doppler shift from a slower toroidal flow in the early phase of a discharge.

The total scattering power, $S$, as shown in the middle panels, is obtained as follows. Since $f < 0$ part of the frequency spectrum, $p(f)$, is almost all due to the stray radiation

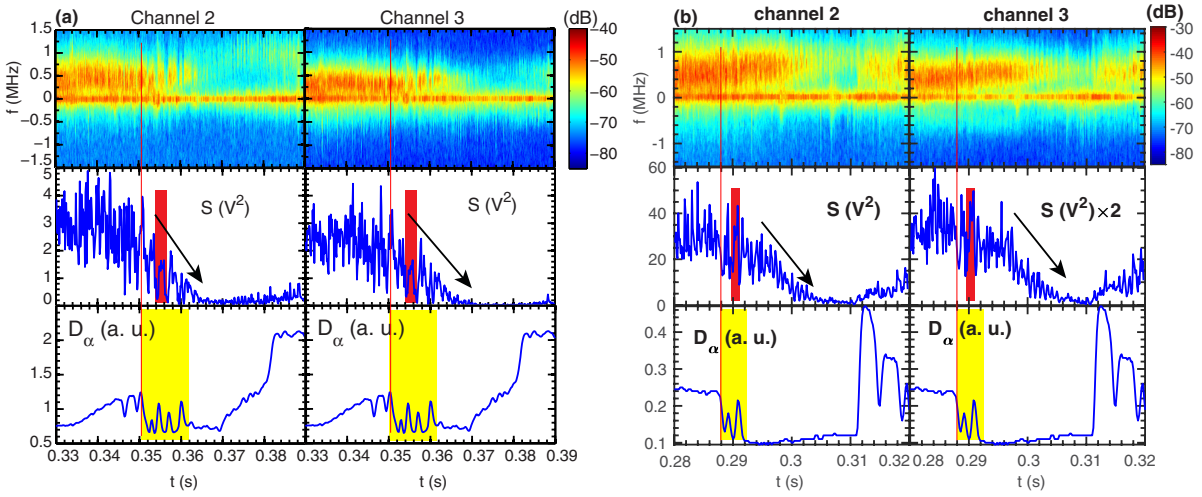


**Figure 4.** (*a*) Shot 139442: spectrogram of scattering channels 2 and 3 (upper panels); the total scattering power, $S$, of channels 2 and 3 (middle panels); divertor $D_\alpha$ emission time trace as reference(bottom panels). (*b*) The same as (*a*) but for shot 141698. Solid vertical lines are drawn to denote the time of the start of the L–H transition. Black arrows are used in the middle panels to denote the overall reduction in the total turbulence spectral power during the intermittent phase. A shaded rectangle in each of the middle panels is used to highlight one of the spectral power spikes in the intermittent phase of the turbulence. A shaded rectangle in each of the bottom panels highlights the dithering phase in the $D_\alpha$ emission after the start of the L–H transition.

whose frequency spectrum should be symmetric with respect to $f = 0$, we subtract $p(-f)$ from $p(f)$ to remove the contribution from the stray radiation to obtain the frequency spectrum of the scattering signal, $p_s(f)$, using $p_s(f) = p(f) - p(-f)$. Since the whole frequency spectrum of the scattering signal is Doppler-shifted to the positive frequency, only the $f > 0$ part of $p_s(f)$ needs to be included in the integration to obtain total scattering power, i.e. $S = \int_{f_0}^{f_1} p_s(f)$ where $f_0 > 0$ is a cutoff frequency and $f_1$ (>0) is the Nyquist frequency. We chose $f_0 = 180$ kHz in the calculation of $S$, and found that as long as $f_0$ is small compared to peak frequency of the scattering frequency spectrum and is large enough to avoid the residual contribution from the stray radiation near $f = 0$, $S$ is not sensitive to the value of $f_0$. We note that $S$ is proportional to the electron-scale density fluctuaton spectral powr of the wavenumber measured by the particular scattering channel (channels 2 and 3 in figure 4). It is clear from the top panels of figure 4(*a*) that before the L–H transition ($t < 350$ ms), the measured turbulence is quasi-stationary. More clearly the middle panels show that although the total scattering power has spikes over time at $t < 350$ ms, the spectral power on average is quite stationary. On the other hand, from $t = 350$ ms, the time of the start of the L–H transition, to $t \approx 365$ ms, the scattering signal spectrograms shown in the upper panels become patchy and intermittent, and this can be more clearly seen in the middle panels, where there are strong decreases and increases in $S$ (i.e. signal spikes in $S$) during the same time period (see the shaded rectangle which highlights one of the spectral power spikes), and overall $S$ clearly decreases during this time period (see the black arrows as guide). We want to point out that in the dithering phase of the divertor $D_\alpha$ emission signal, (highlighted by shaded rectangles in the bottom panels, also shows the same kind of intermittency as the scattering signals shown in the upper and middle panels. More detailed comparisons between the two signals will be presented later in the paper. We also found from the upper and middle panels that there is a turbulence-quiescent time period from $t \approx 365$ ms to about 380 ms when the turbulence is significantly suppressed following the intermittent phase, i.e. from $t \approx 350$ to about 365 ms. Beyond $t \approx 380$ ms, both the upper and middle panels show that the measured turbulence spectral power starts to increase from the significantly suppressed level seen in the turbulence-quiescent phase from $t \approx 365$ ms to about 380 ms. We note that the temporal characteristics of channels 2 and 3 shown in figure 4(*a*) are similar to each other, supporting that the two wavenumbers are measured at the same radial location.

Figure 4(*b*) present the same measured quantities as figure 4(*a*) but for shot 141698. We note that for shot 141698, channels 2 and 3 were configured to measure normalized wavenumbers of $k_\perp \rho_s \sim 7$–8 and $k_\perp \rho_s \sim 5$–6, respectively, across the L–H transition. Comparing figures 4(*b*) with (*a*) for shot 139442, we can also identify a quasi-stationary period before the L–H transition (from $t \approx 280$ ms to about 288 ms with the L–H transition occurring at about 288 ms), an intermittent phase after the start of the L–H transition (from $t \approx 288$ ms to about 305 ms) where electron-scale turbulence show gradual decrease in $S$ with intermittent large relative variations in the total spectral power (see the shaded rectangle which highlights one of the spectral power spikes) and a phase of minimum electron-scale turbulence is found after the intermittent phase (from about $t = 305$ ms to about 310 ms). Note that the time duration of the intermittent phase of shot 141698 (about 17 ms) is comparable to that of shot 139442 (about 15 ms). A recovery phase in the measured turbulence is found after $t \approx 310$ ms. We note that the large spikes in $S$ right after the start of the L–H transition are coincident with the dithering in the divertor $D_\alpha$ signal shown in the bottom panels, the same as seen in figure 4(*a*). Despite all the similarities between the turbulence evolutions of the

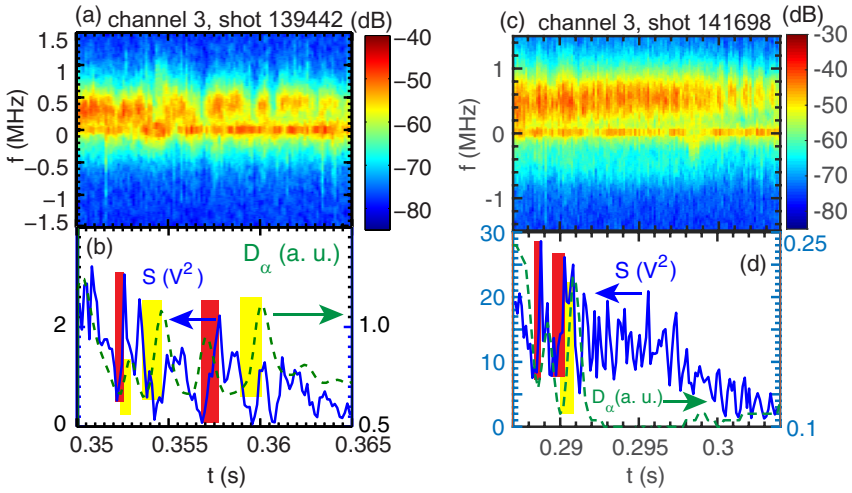


**Figure 5.** (*a*) and (*c*) Spectrogram of scattering channel 3; (*b*) and (*d*): the total scattering power, *S*, of channel 3 (blue solid line) and divertor $D_\alpha$ emission time trace (green dashed line). (*a*) and (*b*) Are for shot 139442, and (*c*) and (*d*) are for shot 141698. In (*b*) and (*d*), shaded rectangles are used to denote the rising time of selected signal spikes in $D_\alpha$ (yellow-shaded) and *S* (red-shaded) with the width of each rectangle.

two discharges, there are also differences. Right after the start of the L–H transition, *S* shown in figure 4(*b*), despite having large variations in amplitude, maintains a quite large finite amplitude even at its minimum (valleys between the spikes). On the other hand, *S* shown in figure 4(*a*) is more severely suppressed at signal valleys during the intermittent phase, even getting close to the turbulence level seen in the turbulence-quiescent phase. Furthermore, while the whole intermittent phase in shot 139442 corresponds to the dithering phase in divertor $D_\alpha$ (figure 4(*a*)), the intermittent phase of shot 141698 seems to have more complicated variations: the beginning part of the intermittent phase corresponds to the dithering in $D_\alpha$ (see $t \approx 288$ ms to about 292 ms in figure 4(*b*)), but a period of large intermittency (where turbulence is severely suppressed at signal valleys) from $t \approx 300$ ms to about 305 ms has no corresponding $D_\alpha$ dithering. Figure 4(*b*) also shows that shot 141698 has a shorter phase of minimum electron-scale turbulence than shot 139442, which is due to an ELM event happening at $t \approx 311$ ms in shot 141698. Lastly, we note that the turbulence recovery phase has different origins in the two discharges. While the recovery phase in shot 139442 (figure 4(*a*)) should be related to equilibrium changes as the plasma evolves further into H-mode, the recovery phase in shot 141698 (figure 4(*b*)) is due to the ELM event happening at $t \approx 311$ ms.

It is clear from figure 4 that all the turbulence suppression happens during the intermittent phase (see the black arrows as guide). Thus, it is important to take a closer view of this phase. Figure 5 shows zoomed-in views of spectrogram of the scattering signal from channel 3 of the high-k scattering system and the total scattering power, *S*, together with the divertor $D_\alpha$ for the two discharges. Comparing figures 5(*a*) and (*c*), we can see that the scattering signal frequency spectrum during the intermittent phase of shot 139442 is more patchy than that of shot 141698, and the intermittency manifests as spectral power valleys and spikes particularly seen in a period from $t \approx 350$ ms to about 362 ms in figure 5(*b*) and in periods from $t \approx 287$ ms to about 292 ms and from $t \approx 300$ ms to about 305 ms in figure 5(*d*). These spectral power valleys, i.e turbulence-suppressed periods, typically last for about 1–2 ms (measured between peaks of two adjacent spectral power spikes). In order to quantify the characteristics of signal spikes, we define the rising time of a spike as the time duration from a signal valley to the next adjacent signal peak (vice versa for the falling time) and the width of a spike as the time duration from one signal valley to the next. Seen in figures 5(*b*) and (*d*), the rising time and falling time of the spectral power spikes are similar, typically 0.5–1 ms (as examples, some rising times are denoted by the widths of shaded rectangles in figures 5(*b*) and (*d*)). Comparing figures 5(*b*) and (*d*) also reveals the widths of the spectral power spikes in figure 5(*b*) have a wider range of 1–3 ms than those in figure 5(*d*), i.e. 1–2 ms. The $D_\alpha$ signal is also plotted in figures 5(*b*) and (*d*) to illustrate more clearly similarities between the $D_\alpha$ dithering and the intermittency *S*. It is seen that the $D_\alpha$ dithering phase has a clear correspondence within the intermittency phase in *S* (see $t \approx 352$ ms to 363 ms in figure 5(*b*) and $t \approx 288$ ms to 292 ms in 5(d)). Widths of the $D_\alpha$ spikes (∼1.5–2.5 ms in figures 5(*b*) and ∼1.5–2 ms in (*d*)) are found to be comparable to those of the nearby spectral power spikes (∼1–3 ms in figures 5(*b*) and ∼1–2 ms in (*d*)). Furthermore, similar rising and falling times (∼0.5–1 ms) are found for the $D_\alpha$ and *S* spikes in both figures 5(*b*) and (*d*). Finally we note that despite the similarities mentioned above, we are yet able to determine if there is a fixed phase correlation between the spikes in *S* and those in $D_\alpha$.

Beyond the detailed temporal evolution of the electron-scale turbulence shown in figure 4 and 5, the high-k scattering system, having five individual scattering channels and relative calibration among them, is able to provide measurements of wavenumber spectrum. The wavenumber spectra of the electron-scale density fluctuations at $t = 332$, 348, 365 and

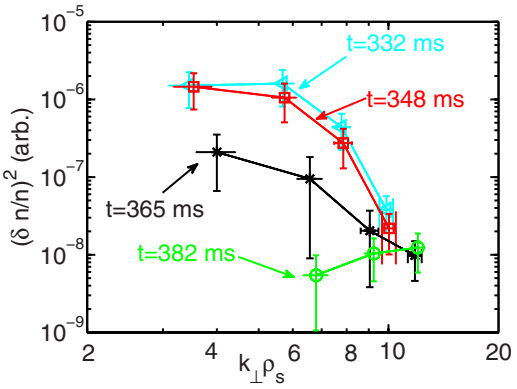


**Figure 6.** Wavenumber spectra measured by the high-k scattering system at $t = 332$ ms (cyan open triangles), 348 ms (red open squares), 365 ms (black asterisks) and 382 ms (green open cicles). Note that both $t = 332$ ms and 348 ms are before the L–H transition, and $t = 365$ ms and 382 ms are after the start of the L–H transition.

382 ms reconstructed using scattering signals from different scattering channels for shot 139442 are shown in figure 6. We chose these four exact MPTS time points to facilitate ray-tracing calculations (which depends on measured electron density profiles) required for calculating measured wavenumbers and their scattering volumes. Given the spectral spikes in the turbulence density fluctuation spectral power seen in figures 4 and 5, these spectra are averaged over about 4 ms to be more time-smoothed. We note that the wavenumber spectral power is not absolutely calibrated but is relatively calibrated, and thus, relative change in wavenumber spectral power and spectral shape can be identified. It can be seen that the wavenumber spectra at $t = 332$ and 348 ms (before the L–H transition) are very similar to each other, consistent with the observation that the observed turbulence is quasi-stationary before the L–H transition. At $t = 365$ ms (after the intermittent phase), the peak spectral power shows a significant drop, i.e. a factor of about 7, compared to those at $t = 332$ and 348 ms before the L–H transition. Further into H-mode at $t = 382$ (at the end of turbulence-quiescent period), the turbulence spectral power is further reduced, i.e. an order of magnitude drop in spectral power seen at $k_\perp\rho_s \sim 7$ compared with that at $t = 365$ ms. Note that at $t = 382$ ms, only three channels are used since the scattering signal from channel 4 is below noise level. Figure 6 also demonstrates clearly that a significant reduction in turbulence spectral power is only observed at smaller wavenumbers, i.e. $k_\perp\rho_s < 9$–10, across the L–H transition, beyond which the spectral power remains relatively unchanged. We would like to point out that a significant reduction in the turbulence spectral power at $k_\perp\rho_s < 9$–10 due to a change in plasma condition was also observed in NBI-heated L-mode plasmas where the reduction in the peak wavenumber spectral power was found to be correlated with an increase in the $E \times B$ shear [39], in an NBI-heated H-mode plasma where the suppression of electron-scale turbulence was found to be due to large density gradient [19] and also in NSTX RF-heated L-mode plasmas where electron-scale turbulence showed an immediate drop at smaller wavenumber after RF-heating cessation [40]. These observations implies that smaller wavenumbers (still in the electron-scale range) are more responsible for electron thermal transport, which is consistent with theoretical expectations. We also note that despite this consistency, it is not yet understood the reason why a significant reduction in the turbulence spectral power is only observed for $k_\perp\rho_s < 9$–10, which is subject to further investigation. We point out that although not shown here, the change in wavenumber spectrum across the L–H transition in shot 141698 is qualitatively similar to that of shot 139442 shown in figure 6.

Finally, we note that the comparison of shots 139442 and 141698 above is to emphasize similarities in the electron-scale turbulence evolution across the L–H transition in both shots, despite the difference in plasma parameters and in the trigger of the L–H transition (the L–H transition in shot 139442 was triggered by a NBI power step-up and the L–H transition in shot 141698 is spontaneous). In particular, the evolution of electron-scale turbulence for both shots is shown to have four similar phases, and both shots show that the suppression of electron-scale turbulence after the start of the L–H transition is a gradual process happening on a tens-of-ms time scale. The comparison demonstrates that the observed electron-scale turbulence evolution report in this paper is a reproducible phenomenon. In the rest of the paper, we choose to focus on shot 139442 for further detailed analysis (including comparisons with ion-scale turbulence measurements and linear gyrokinetic stability analysis), due to the similar evolution of the electron-scale turbulence in the two shots and the fact that only shot 139442 has comprehensive ion-scale turbulence measurements, i.e. both BES and GPI measurements, in the edge of the plasma.

### *3.3. Comparison with ion-scale turbulence measurements*

Ion-scale turbulence measurements at the plasma edge were also available from both BES [30] and GPI diagnostics [31] in shot 139442. Having presented the evolution of electron-scale turbulence across the L–H transition, it is interesting to compare electron-scale turbulence measurements with ion-scale turbulence measurements. We note that the high-k measurement region in shot 139442 is $r/a \approx 0.71$–0.84, while BES and GPI measurements were taken at $r/a \gtrsim 0.81$. Although there is no exact overlap between the high-k measurement region and BES/GPI measurement region, comparing turbulence evolution at different locations at the plasma edge should still provide insight on the correlation between electron and ion-scale turbulence, e.g. the temporal sequence of turbulence suppression at different locations after the start of the L–H transition. In order to make the comparison, we chose one BES channel located at $R = 142$ cm (on the top of the pedestal) and GPI measurement at $R = 144$ cm (in the pedestal region). Figure 7 shows the spectrogram of the scattering signal from scattering channel 3 (measuring $k_\perp\rho_s \sim 5$–7) (figure 7(*a*)), the spectrogram of the ion-scale density fluctuation measured by the BES channel (figure 7(*b*)) and the total scattering power, $S$, together with the ion-scale density fluctuation power measured by the BES channel (figure 7(*c*)). The ion-scale density fluctuation

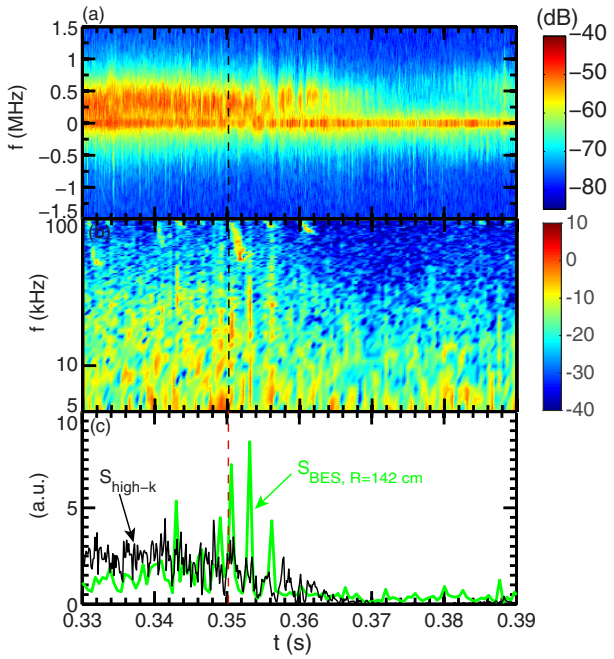


**Figure 7.** (*a*) Spectrogram of scattering channel 3; (*b*) spectrogram of a BES channel at $R = 142$ cm; (*c*) total scattering power ($S_{\mathrm{high-k}}$) together with ion-scale density fluctuation power measured by a BES channel at $R = 142$ cm, $S_{\mathrm{BES},R=142\ \mathrm{cm}}$.

power in figure 7(*c*) is obtained by integrating the frequency spectrum in figure 7(*b*) from 8 kHz to 45 kHz, where the upper frequency limit is chosen to exclude some MHD modes at some higher frequencies. Comparing the two spectrograms in figures 7(*a*) and (*b*), we can see that although the BES spectrogram is more patchy than the electron-scale turbulence signal, a quasi-stationary phase can also be identified before the L–H transition at about 350 ms. This quasi-steady-state phase can be more clearly seen in the ion-scale density fluctuation power shown in figure 7(*c*). After the start of the L–H transition, an overall decrease in ion-scale turbulence can be seen in both figures 7(*b*) and (*c*) with large intermittency, corresponding to the aforementioned intermittent phase in electron-scale turbulence. Furthermore, a turbulence-quiescent phase (from about 368 ms to about 376 ms) and recovery phase ($t > 376$ ms) can also be identified in figures 7(*b*) and (*c*), although the turbulence-quiescent phase is shorter than that of electron-scale turbulence. Since the BES signal is proportional to density fluctuation, we found that the normalized density fluctuation, $\tilde{n}_e/n_e$, is about 2.9% before the L–H transition and is about 0.94% into H-mode (averaged between $t = 365$ and 390 ms).

The normalized GPI fluctuation level, $\tilde{I}/\bar{I}$, is plotted together with $S$ of the scattering channel 3 in figure 8, where $\tilde{I}$ is the RMS value of the GPI signal in a small area around $R = 144$ cm over a time period of 130 $\mu$s and $\bar{I}$ is the mean value of the GPI signal in the same area and same time period (additional average of $\tilde{I}/\bar{I}$ over 0.5 ms was used to smooth the signal). Comparison of $\tilde{I}/\bar{I}$ and $S$ immediately shows that a quasi-steady-state phase in $\tilde{I}/\bar{I}$ can also be seen before the L–H transition as seen in $S$. After the start of the L–H transition,

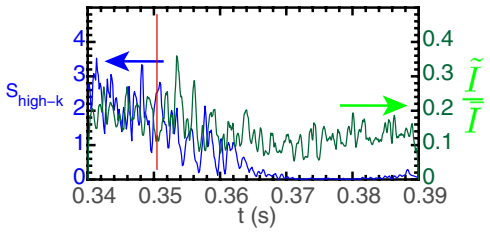


**Figure 8.** Normalized GPI fluctuations, $\tilde{I}/\bar{I}$, at $R = 144$ cm as a function of time (green) together with $S$ from the scattering channel 3 (blue). The vertical solid line denotes the time point of the L–H transition.

$\tilde{I}/\bar{I}$ seems to have a brief increase in amplitude before starting to decrease in overall amplitude, and in this declining phase, large intermittency can also be seen (from $t \approx 350$ ms to about 365 ms), corresponding to the intermittent phase seen in $S$. Similar to the BES measurement, the phase of minimum $\tilde{I}/\bar{I}$ is quite short (from about 365 ms to about 373 ms), after which $\tilde{I}/\bar{I}$ starts to increase as plasma evolves further into H-mode. In contrast, $S$ stays low for longer time period until $t \approx 380$ ms. We would like to point out that although $\tilde{I}/\bar{I}$ shown here is measured at $R = 144$ cm in the ETB region, we do not see a sharp suppression of turbulence on the 100 $\mu$s time scale and staying low thereafter (even in $\tilde{I}/\bar{I}$ without the additional 0.5 ms smoothing) as observed in previous experiments [8–10, 12]. Comparing the measured ion-scale turbulence and electron scale turbulence from edge into core, we found that none of them is obviously leading in the response to the L–H transition and that the overall turbulence suppression after the start of the L–H transition at different radial locations seems to start at the same time, i.e. the time of the L–H transition, and is a gradual process happening on a tens-of-ms time scale. Since electron and ion-scale turbulence would drive anomalous transports, we would also expect that particle and thermal confinement respond to the L–H transition immediately (just like the observed turbulence) and increase on the same time scale as the turbulence evolves after the start of the L–H transition. We note that fast profile diagnostics (like those used in [8–10, 12]) are required to experimentally determine the time scale of plasma confinement evolution after the start of the L–H transition but were not available in the experiments reported in this paper. Future experiments with fast profile diagnostics will be conducted on NSTX-U to further investigate this issue.

## 4. Linear gyrokinetic stability analysis

In this section, we present linear gyrokinetic stability analysis with experimental profiles at $t = 348$ ms (before the L–H transition), 365 ms (right after the intermittent phase) and 382 ms (around the end of the phase of minimum turbulence) which are three exact MPTS time points. The GS2 gyrokinetic code [41] was used to carry out the linear stability analysis. We note that the GS2 code is an initial value gyrokinetic code which, with linear mode, finds the fastest growing mode for a given pair of poloidal and radial wavenumbers (note that

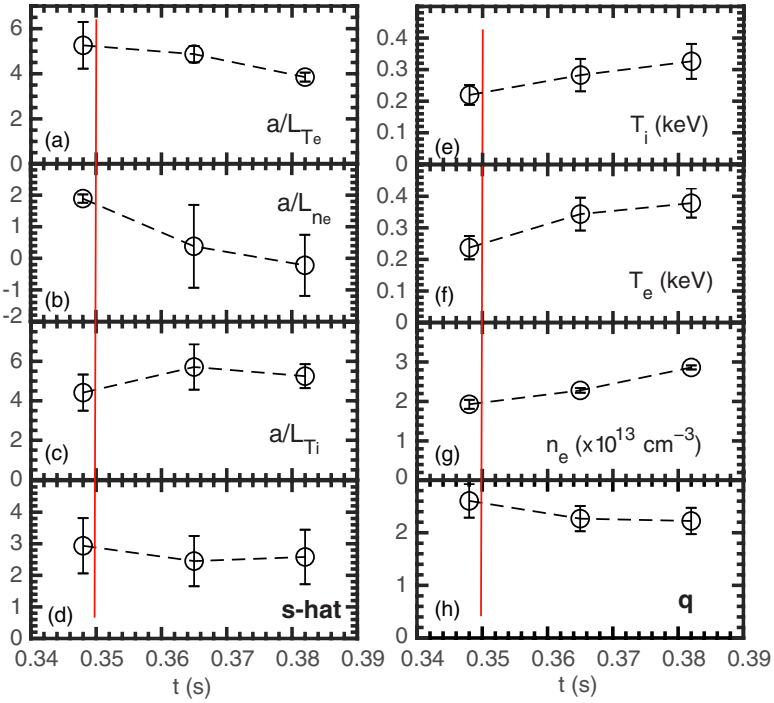


**Figure 9.** Eight equilibrium quantities averaged in the high-k measuring region at three exact MPTS time points ($t = 348$, 365 and 382 ms) for shot 139442: (*a*) $a/L_{T_e}$, (*b*) $a/L_{n_e}$, (*c*) $a/L_{T_i}$, (*d*) $\hat{s}$, (*e*) $T_i$, (*f*) $T_e$, (*g*) $n_e$, (*h*) $q$. The errorbars denote the spatial variation of these equilibrium quantities in the high-k measurement region. The error in $a/_{T_e}$ from MPTS measurement is about 15%. The red vertical solid lines denote the time of the start of the L–H transition. Note that all gradients are normalized to $a$. Also note the ion temperature and its gradients at the MPTS times point are calculated from the nearest CHERS measurement time points.

radial wavenumber was set to zero to find the most unstable modes). We use local Miller equilibrium [42] in these GS2 linear simulations, and electromagnetic effects, electron and ion collisions and carbon impurity are included. Numerical convergence has been verified. In the rest of this section, we focus on shot 139442 for which we have carried out extensive linear stability analysis.

Since local linear stability is determined by local equilibrium quantities only, how equilibrium quantities (particularly instability-driving gradients) in the high-k measurement region vary across the L–H transition would be informative for understanding linear stability analysis result. Thus, temporal evolutions of eigtht equilibrium quantities across the L–H transition are plotted at the three exact MPTS time points in figure 9. The errorbars in the figure represent profile variations in the high-k measurement region. Electron temperature, $T_e$ (figure 9(*f*)), electron density, $n_e$ (figure 9(*g*)), the normalized electron density gradient, $a/L_{n_e}$ (figure 9(*b*)), and normalized electron temperature gradient, $a/L_{T_e}$ (figure 9(*a*)), are obtained from the MPTS profiles. Ion temperature, $T_i$ (figure 9(*e*)), and the normalized ion temperature gradient, $a/L_{T_i}$ (figure 9(*c*)), are obtained using the CHERS measurements (both active and passive) [43]. $a$, $q$ (figure 9(*h*)) and $\hat{s}$ (figure 9(*d*)) are obtained from LRDFIT (LR circuit model with data FITting capabilities) equilibrium reconstructions constrained by magnetic pitch angle measurements from a motional Stark effect (MSE) diagnostic [44, 45]. It can be immediately seen that the largest change is in $a/L_{n_e}$ which decreased from about 2 to about 0. Note this decrease in $a/L_{n_e}$ is due to the formation of density ear seen in figure 3. Significant changes in $T_e$, $T_i$ and $n_e$ are also observed each with an increase ranging from 45% to 60%. $a/L_{T_e}$, which is the driving gradient for ETG modes, decreased after the start of the L–H transition by 30%, and the change of $a/L_{T_i}$ is not monotonic across the L–H transition with a variation up to 30%. $\hat{s}$ and q show the smallest variation (less than 20%) across the L–H transition. Furthermore, with $T_e/T_i$ increased after the start of the L–H transition judging from figures 9(*e*) and (*f*) and $a/L_{T_e}$ decreased, we would expect that ETG mode linear growth rate to decrease after the start of the L–H transition if ETG modes are unstable.

The linear analysis was carried out for a wide range of poloidal wavenumbers, from the ion scale ($k_\theta \rho_s$ as low as 0.3) to the electron scale ($k_\theta \rho_s$ up to 60) using the equilibrium quantities at $R = 138$ cm which is about the center of the high-k measurement region. Figure 10(*a*) shows that a wide range of $k_\theta$ modes is linearly unstable. In the ion scale, i.e. $k_\theta \rho_s < 1$, the peak of the linear growth rate, $\gamma$, is about 0.3–0.5 $C_s/a$ for the three time points and is smallest at the last time point, i.e. $t = 382$ ms, with the peak linear growth rate decreased by about 50% from the earlier time points. In contrast, the peak linear growth rate in the electron scale, i.e. $k_\theta \rho_s > 1$, has much larger reduction across the L–H transition with a reduction in the peak linear growth rate by more than an order of magnitude from $t = 348$ ms to 382 ms. Furthermore, the reduction in the linear growth is broad across the whole electron-scale wavenumbers. In figure 10(*b*), the wave propagation direction,

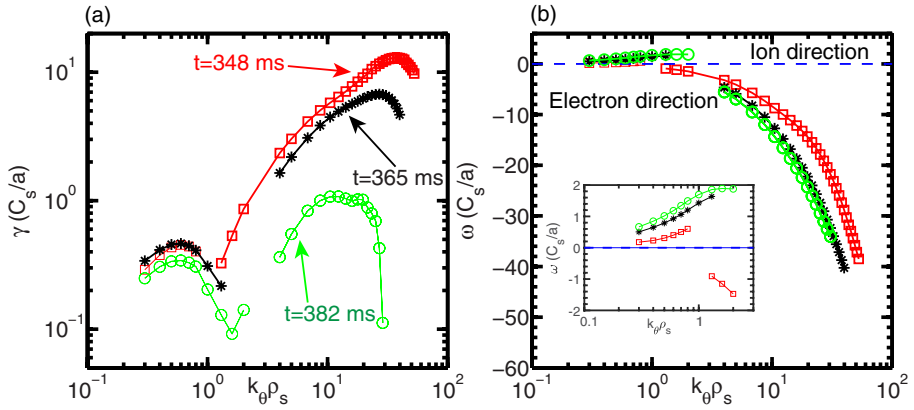


**Figure 10.** (*a*) Linear growth rate, $\gamma$, and (*b*) mode frequency, $\omega$, spectra at $t = 348$ ms (red open square), $t = 365$ ms (black asterisk) and $t = 382$ ms (green open circle) at $R = 138$ cm (about the center of the high-k measurement region). Note that modes with $\omega < 0$ propagate in the electron diamagnetic drift direction and $\omega > 0$ denotes the ion diamagnetic drift direction. The insert in (*b*) shows a zoomed-in portion of the real frequency spectra in the ion scale (from $k_\theta \rho_s = 0.1$ to 1). The horizontal dashed lines denote the line of zero for reference.

judged from the sign of the real frequency, provides the information on the nature of the modes. It can be seen that the ion-scale modes propagate in the ion diamagnetic direction (more clearly seen in the insert in figure 10(*b*)), showing that the ion-scale modes are most likely to be ion temperature gradient (ITG) driven mode. On the other hand, electron-scale modes propagate in the electron direction and are identified as ETG modes. Thus, from figure 10 we can conclude that linear ETG mode is significantly stabilized after the start of the L–H transition and further into H-mode, which is consistent with the experimentally observed reduction of the electron-scale wavenumber spectral power at $k_\perp \rho_s \leqslant 9$–10 into H-mode seen in figure 6 and confirms our expectation from equilibrium evolutions across the L–H transition shown in figure 9. However, we note that the much smaller variation in the spectral power at $k_\perp \rho_s > 9$–10 after the start of the L–H transition (compared to the spectral power at $k_\perp \rho_s \leqslant 9$–10) shown in figure 6 cannot be explained by the change in the ETG linear growth rates shown in figure 10(*a*), which is subject to future studies. We also note that although the observed overall decrease in $S$ after the start of the L–H transition (see the middle panels of figures 4(*a*), (*b*) and 5(*b*), (*d*)) is consistent with the linear ETG stabilization, the large intermittency in the electron-scale turbulence after the start of the L–H transition can only come from nonlinear effects. Furthermore, although not shown here, the maximum ETG linear growth rate in shot 141698 is also found to be significantly reduced after the start of the L–H transition, qualitatively similar to shot 139442 and consistent with the observed overall decrease in the electron-scale turbulence spectral power after the start of the L–H transition.

Another way to assess the ETG stability across the L–H transition is to study the change in the normalized linear critical electron temperature gradient, $a/L_{T_{e,critic}}$. We have also used the GS2 code to determine $a/L_{T_{e,critic}}$ at each time points used in figure 10, following the procedure used in [46]: growth rates of a range of unstable poloidal wavenumbers are calculated with several different temperature gradients, and linear extrapolation of the growth rate of the most unstable mode determines

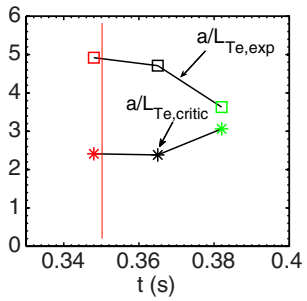


**Figure 11.** Normalized experimental electron temperature gradient, $a/L_{T_{e,exp}}$, (open squares) and the normalized linear critical electron temperature gradient, $a/L_{T_{e,critic}}$ (asterisks) at three exact MPTS time points: 348 ms, 365 ms and 382 ms. The red vertical solid line denotes the time of the start of the L–H transition.

the critical temperature gradient. In figure 11, $a/L_{T_{e,critic}}$ calculated for the center of the high-k measurement region, i.e. $R = 138$, is shown for the three MPTS time points across the L–H transition together with the normalized experimental $T_e$ gradient, $a/L_{T_{e,exp}}$, at the same location at each time. The difference between $a/L_{T_{e,exp}}$ and $a/L_{T_{e,critic}}$ determines stability of the ETG modes: the smaller the difference, the smaller the linear growth rate (more suppression in ETG turbulence would be expected in the nonlinear phase). Figure 11 clearly shows that the difference between $a/L_{T_{e,critic}}$ and $a/L_{T_{e,exp}}$ becomes smaller after the start of the L–H transition and, at $t = 382$ ms, ETG modes are close to marginal stability. With the comparison of absolute values of $a/L_{T_{e,critic}}$ and $a/L_{T_{e,exp}}$, figure 11 also demonstrates that both the decrease in $a/L_{T_{e,exp}}$ and the increase in $a/L_{T_{e,critic}}$ lead to the stabilization of ETG into H-mode.

As shown in figure 10, the maximum linear growth rate of ITG modes in the center of the high-k measurement region does not vary much across the L–H transition. However, this does not mean ITG turbulence is unchanged across the L–H transition, since ITG turbulence is more prone to $E \times B$ shear than ETG turbulence. We can evaluate the effect of $E \times B$ shear on ITG turbulence across the L–H transition

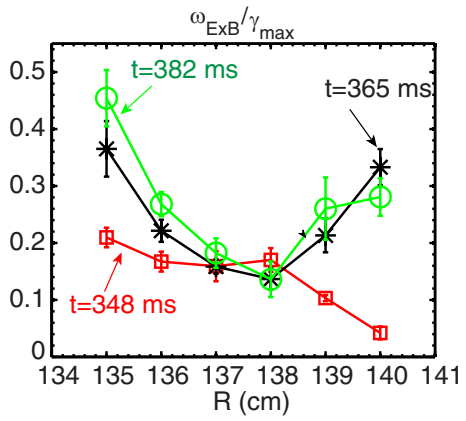


**Figure 12.** The radial profiles of the ratio between the Waltz-Miller $E \times B$ shearing rate, $\omega_{E\times B,\mathrm{WM}}$, and the maximum linear growth rate of ITG mode, $\gamma_{\max}$, using the for three MPTS measurement time points.

using gyrokinetic simulations. To rigourously model $E \times B$ shear effect, nonlinear gyrokinetic simulations are required. However, linear stability analysis can actually provide some initial assessment of the $E \times B$ shear effect in the experiment, motivated by studies on $\omega_{E\times B}$ and linear growth rate reported in [47, 48]. Figure 12 plots the radial profiles of the ratio between the Waltz-Miller $E \times B$ shearing rate, $\omega_{E\times B,\mathrm{WM}}$, and the maximum linear growth rate of ITG modes, $\gamma_{\max}$, for three MPTS measurement time points. We note that the larger $\omega_{E\times B,\mathrm{WM}}/\gamma_{\max}$, the stronger the $E \times B$ shearing effect. It can be seen in figure 12 that the shearing effect doe not change much around the center of the high-k measurement region from $R = 137$ cm to 138 cm across the L–H transition, while having the largest change toward the plasma edge (up to a factor of about 8 increase at $R = 140$ cm) and a moderate increase toward plasma core (up to a factor of about 2 at $R = 135$ cm). This observation on the enhanced $E \times B$ shearing effect on ITG turbulence shows that the $E \times B$ shearing stabilization effect not only occurs in the ETB as well known, but also at smaller radii than the ETB (note that ETB locates at $R \gtrsim 143$ cm). However, there are also radial locations (i.e. around center of the high-k measurement region) where $E \times B$ shearing effects on ITG mode do not change much across the L–H transition, indicating that ITG turbulence is not suppressed by the $E \times B$ shear around the center of the high-k measurement region after the start of the L–H transition. Since ITG turbulence is not likely being suppressed around the center of the high-k measurement region after the start of the L–H transition, it is also unlikely that the observed stabilization of electron-scale turbulence after the start of the L–H transition is due to the $E \times B$ shear stabilization of ion-scale turbulence through the possible cross-scale nonlinear interaction between ion-scale and electrons-scale turbulence as suggested in [39, 49]. We note that to fully investigate $E \times B$ shear effects on ITG turbulence and the possible cross-scale nonlinear interaction between ion-scale and electrons-scale turbulence in the high-k measurement region, nonlinear multi-scale gyrokinetic simulations are needed and will be subjected to future studies.

## 5. Summary and discussion

In this paper, we have presented the first detailed observation of the evolution of electron-scale turbulence across the L–H transition in NSTX NBI-heated plasmas with a 280 GHz coherent microwave scattering system (the high-k scattering system [30]). The L–H transition, across which the observations were made, occurred during the current flattop of the discharges, and the late L–H transition is featured with a much larger toroidal flow, compared to cases with the L–H transition occurring during the earlier current ramp-up phase, and facilitates the electron-scale turbulence measurement by introducing a large Doppler frequency shift. Successful measurement of electron-scale turbulence relies on this large Doppler frequency shift to differentiate scattering signals from stray radiation. The high-k scattering system has the unique capability of making radially localized turbulence measurements due to its innovative tangential scattering scheme [28]. Although the measurement location of electron-scale turbulence in these plasmas was located around $r/a \approx 0.71$–$0.88$ which is outside of the ETB, located at $r/a \gtrsim 0.89$–$0.9$, we still observed distinct effects on electron-scale turbulence due to the L–H transition. It was observed that the evolution of the electron-scale turbulence can be classified into four phases. One quasi-stationary phase is observed before the L–H transition, followed by a intermittent phase after the start of the L–H transition. The measured electron-scale density fluctuation spectral power ($\propto S$) decreases on a 10–15 ms time scale in the intermittent phase with a large intermittency characterized by large rise and fall in turbulence density fluctuation spectral power on a much faster time scale (0.5–1 ms) than the overall decrease of turbulence density fluctuation spectral power. Between the large rise and fall of electron-scale turbulence, there exist brief periods (on 1–2 ms time scale) of minimum turbulence (shown as spectral power valleys). After the intermittent phase, electron-scale turbulence becomes significantly suppressed for about 5–15 ms (turbulence-quiescent phase), and after this, turbulence spectral power starts to recover again but never reached the same magnitude in the L-mode. Analyzing the temporal evolution of the measured electron-scale wavenumber spectra across the L–H transition shows that a significant reduction in the electron-scale turbulence spectral power is only observed at lower wavenumbers, namely $k_\perp \rho_s \leqslant 9$–$10$, which is also seen in different operational NSTX scenarios due to different stabilization mechanisms. However, the much smaller variation in the spectral power at $k_\perp \rho_s > 9$–$10$ after the start of the L–H transition (compared to $k_\perp \rho_s \leqslant 9$–$10$) is not yet understood, which is subject to future studies. Comparing ion-scale turbulence measurements from BES and GPI with the measured electron-scale turbulence shows that although these measurements were taken at different radial locations of the plasma (i.e. the high-k measurement region at $R \approx 135.5$–$141$ cm, BES measurement at H-mode pedestal top, $R \approx 142$ cm, and GPI measurement in the ETB, $R \approx 144$ cm), the evolution of ion-scale turbulence is similar to that of electron-scale turbulence with the same four phases. On the other hand, ion-scale turbulence measured by both BES and GPI seem to have a

much shorter turbulence-quiescent phase than electron-scale turbulence, which means that ion-scale turbulence starts to recover from the suppression before the measured electron-scale turbulence.

Linear gyrokinetic simulations were carried out with the GS2 code [41] with experimental equilibrium profiles at the location of the electron-scale turbulence measurement. We show that there is a wide range of modes that are linearly unstable from ion scale to electron scale with ITG modes in the ion scale and ETG modes in the electron scale. While the maximum ion-scale linear growth rate shows a slight decrease into H-mode, the maximum electron-scale linear growth rate is reduced by more than an order of magnitude into H-mode, and particularly at $t = 382$ ms, ETG modes are close to marginal stability. This dramatic reduction in the maximum electron-scale linear growth rate in the high-k measurement region after the start of the L–H transition can be attributed to both a decrease in the experimental $a/L_{T_e}$ and an increase in $a/L_{T_{e,critic}}$ and is consistent with the overall reduction in $S$ in the intermittent phase seen in figure 4. Compared with the variation in the wavenumber spectra after the start of the L–H transition (see figure 6), this reduction of the maximum electron-scale linear growth rate is also consistent with the large reduction in the peak spectral power at $k_\perp \rho_s \leqslant 9$–10 after the start of the L–H transition but cannot explain the much smaller variation in the spectral power observed at $k_\perp \rho_s > 9$–10. These observations imply that ETG modes could be important for driving plasma transport in NSTX plasmas and, thus, its suppression is required for reaching higher H factor after the start of the L–H transition. While ion-scale turbulence can be suppressed by the $E \times B$ shear, ETG turbulence is not sensitive to $E \times B$ shear due to its much higher linear growth rate, and our linear analysis show that other equilibrium profile variations seem to be enough to explain the observed electron-scale turbulence stabilization. Nonlinear gyrokinetic simulations are planned to assess the role of ETG turbulence in driving thermal transport in these plasmas. The nonlinear effect of the $E \times B$ shear on ITG modes in the high-k measurement region is studied by examining the ratio of between the Waltz-Miller $E \times B$ shearing rate, $\omega_{E\times B,\mathrm{WM}}$, and the maximum linear growth rate of ITG mode, $\gamma_{\max}$ [47, 48]. We found that the ratio is relatively unchanged in the center of the high-k measurement region, meaning that ITG modes are less affected there, and the stabilizing effect of the $E \times B$ shear on ITG modes are much stronger away from the high-k measurement region, both towards the plasma core and the edge. This implies that stabilizing ion-scale turbulence may not be the source of electron-scale turbulence stabilization if there exist nonlinear interaction between ion-scale and electrons-scale turbulence as suggested in [39, 49].

Finally, we would like to emphasize that since the time resolution in the spectrogram is about 270 $\mu$s (thus for $S$ as well) for electron-scale turbulence in figure 4, 5, 7 and 8, the observed fast change (on a 0.5–1 ms time scale) in the turbulence spectrum is well-resolved (we found that a higher time resolution in the spectrogram did not make a difference), and thus, we do not observe the fast turbulence suppression on 100 $\mu$s time scale as observed in the previous observations [8–10, 12]. One the other hand, our observation of turbulence suppression after the start of the L–H transition is more similar to the slow stage of turbulence suppression observed in [9], which happens on a tens-of-ms times scale. However, the large intermittency observed during the turbulence suppression in these NSTX observation is a distinctly different feature from previous observations. In addition, with regard to the response to the L–H transition, none of the measured ion-scale turbulence and electron scale turbulence from edge into core is obviously leading, meaning that the suppression seems to start at the same time.

## Acknowledgments

The authors would like to thank the NSTX team for the excellent technical support for this work. This manuscript is based upon work supported by the U.S. Department of Energy, Office of Science, Office of Fusion Energy Sciences, and has been authored by Princeton University under Contract No. DE-AC02-09CH11466 with the U.S. Department of Energy. This work was also supported by the U.S. Department of Energy under Contract Nos. DE-AC02-76CH03073, DE-FG03-95ER54295, and DE-FG03-99ER54518.

## ORCID iDs

Y. Ren https://orcid.org/0000-0003-4571-9046
W. Guttenfelder https://orcid.org/0000-0001-8181-058X

## References

[1] Wagner F. *et al* 1982 *Phys. Rev. Lett.* **49** 1408
[2] Wagner F. 2007 *Plasma Phys. Control. Fusion* **49** B1
[3] Biglari H. *et al* 1990 *Phys. Fluids* B **2** 1
[4] Shaing K.C. and Crume E.C. 1989 *Phys. Rev. Lett.* **63** 2369
[5] Kim E.-J. and Diamond P.H. 2003 *Phys. Plasmas* **10** 1698
[6] Xu G.S. *et al* 2011 *Phys. Rev. Lett.* **107** 125001
[7] Schmitz L. *et al* 2012 *Phys. Rev. Lett.* **108** 155002
[8] Matsumoto H. *et al* 1992 *Plasma Phys. Control. Fusion* **34** 615
[9] Philipona R. *et al* 1993 *Phys. Fluids* B **5** 87
[10] Rettig C. *et al* 1993 *Nucl. Fusion* **33** 643
[11] Basse N.P. *et al* 2002 *Phys. Plasmas* **9** 3035
[12] Morisaki T. *et al* 1996 *J. Phys. Soc. Japan* **65** 133
[13] McKee G.R. *et al* 2008 *Plasma Fusion Res.* **2** 1025
[14] Zweben S.J. *et al* 2010 *Phys. Plasmas* **17** 102502
[15] Diallo A. *et al* 2017 *Nucl. Fusion* **57** 066050
[16] Smith D. unpublished results
[17] Lee Y.C. *et al* 1987 *Phys. Fluids* **30** 1331
[18] Mazzucato E. *et al* 2008 *Phys. Rev. Lett.* **101** 075001
[19] Ren Y. *et al* 2011 *Phys. Rev. Lett.* **106** 165005
[20] Ren Y. *et al* 2012 *Phys. Plasmas* **19** 056125
[21] Wang W.X. *et al* 2010 *Phys. Plasmas* **17** 072511
[22] Petty C. *et al* 2015 *Nucl. Fusion* **56** 016016
[23] Pan C. *et al* 2017 *Nucl. Fusion* **57** 036018
[24] Lin L. *et al* 2009 *Phys. Plasmas* **16** 012502
[25] Philipona R. *et al* 1990 *Rev. Sci. Instrum.* **61** 3007
[26] Saffman M. *et al* 2001 *Rev. Sci. Instrum.* **72** 2579
[27] Smith D.R. *et al* 2008 *Rev. Sci. Instrum.* **79** 123501
[28] Mazzucato E. 2003 *Phys. Plasmas* **10** 753
[29] Ono M. *et al* 2000 *Nucl. Fusion* **40** 557
[30] Smith D.R. *et al* 2012 *Rev. Sci. Instrum.* **83**
[31] Maqueda R.J. *et al* 2003 *Rev. Sci. Instrum.* **74** 2020

[32] Yuh H.Y. *et al* 2011 *Phys. Rev. Lett.* **106** 055003
[33] Mazzucato E. *et al* 2009 *Nucl. Fusion* **49** 055001
[34] Guttenfelder W. and Candy J. 2011 *Phys. Plasmas* **18** 022506
[35] Hawryluk R.J. 1981 *Physics of Plasma Close to Thermonuclear Conditions* (New York: Pergamon)
[36] LeBlanc B.P. *et al* 2003 *Rev. Sci. Instrum.* **74** 1659
[37] Zohm H. 1994 *Phys. Rev. Lett.* **72** 222
[38] Menard J. *et al* 2011 *IEEE/NPSS 24th Symp. on Fusion Engineering (Chicago, IL, 26–30 June 2011)* pp 1–8
[39] Ren Y. *et al* 2013 *Nucl. Fusion* **53** 083007
[40] Ren Y. *et al* 2015 *Phys. Plasmas* **22** 110701
[41] Kotschenreuther M. *et al* 1995 *Comput. Phys. Commun.* **88** 128
[42] Miller R.L. *et al* 1998 *Phys. Plasmas* **5** 973
[43] Bell R.E. 2006 *Rev. Sci. Instrum.* **77** 10E902
[44] Menard J.E. *et al* 2006 *Phys. Rev. Lett.* **97** 095002
[45] Levinton F.M. *et al* 2007 *Phys. Plasmas* **14** 056119
[46] Jenko F. *et al* 2001 *Phys. Plasmas* **8** 4096
[47] Burrell K.H. 1997 *Phys. Plasmas* **4** 1499
[48] Kinsey J.E. *et al* 2007 *Phys. Plasmas* **14** 102306
[49] Jenko F. 2004 *J. Plasma Fusion Res. SERIE* **6** 11